Research Square

Preprints are preliminary reports that have not undergone peer review.
They should not be considered conclusive, used to inform clinical practice,
or referenced by the media as validated information.

Peroxymonosulfate activation by ultra-dispersed Co3O4 nanosheets for efficient 4-nitrophenol degradation

zixuan xu
Ningxia Normal University
haoran guo
Ningxia Normal University
he li
Ningxia Normal University
chunlong ma
Ningxia Normal University
hui xu
Ningxia Huayu Chemical Co., Ltd.
haijiao xie
Hangzhou Yanqu Information Technology Co., Ltd.
xiaoni qi
Ningxia Normal University
zhenliang li
1051289681@qq.com
Ningxia Normal University

Research Article

Keywords: Co3O4 nanosheet, Photocatalytic degradation, 4-nitrophenol, Organic pollutants, Peroxymonosulfate

Posted Date: May 21st, 2026

DOI: https://doi.org/10.21203/rs.3.rs-9598560/v1

License: This work is licensed under a Creative Commons Attribution 4.0 International License.
Read Full License

Additional Declarations: No competing interests reported.

Peroxymonosulfate activation by ultra-dispersed Co_3O_4 nanosheets for efficient 4-nitrophenol degradation

ABSTRACT

Traditional Co_3O_4 nanosheets tend to aggregate, leading to the concealment of active sites and causing a decrease in pollutant removal efficiency. In this study, waste fiber was employed as a sacrificial template to prepare highly ultra-dispersed Co_3O_4 (U-Co_3O_4) nanosheets with abundant exposed active sites. In a typical reaction, 4-NiP (40 mg/L) was almost completely degraded in 10 min by the activation of PMS (1.0 mmol) using U-Co_3O_4 (20 mg/L). It was found that U-Co_3O_4 nanosheets exhibited outstanding catalytic performance toward 4-nitrophenol (4-NiP) than conventional Co_3O_4. Moreover, the U-Co_3O_4 can degrade various pollutants within 10 minutes. Moreover, nine organic pollutants including 4-nitrophenol (4-NiP), 2-chloro-4-nitrophenol (2C4Nip), 2-chloro-6-nitrophenol (2C6Nip), tetracycline (TC), doxycycline (DOX), methyl orange (MO), oxytetracycline (OTC), methylene blue (MB), and methyl red (MR)were utilized to investigate the generality of catalyst. The possible interface mechanism of PMS activation by U-Co_3O_4 was proposed, the (111) facets of Co_3O_4 can activate PMS efficiently generating •OH, $SO_4^{\bullet -}$, $^1O_2$, and $O_2^{\bullet -}$. This work provides a new strategy for preparing U-Co_3O_4 nanosheets catalysts via a sacrificial template method for efficient wastewater treatment.

KEYWORDS: Co_3O_4 nanosheet, Photocatalytic degradation, 4-nitrophenol, Organic pollutants, Peroxymonosulfate

1. Introduction

In recent years, numerous techniques have been proposed for water treatment, including adsorption method, electro/photocatalytic degradation, and advanced oxidation processes (AOPs). Among these, AOPs were regarded as an effective technology for wastewater decontamination[1]. The various AOPs have been extensively investigated, such as Fenton-based processes (H_2O_2)[2], photocatalytic ozonation (O_3)[3], periodate (IO_4^-), peracetic acid ($CH_3C(O)OOH$)[4], sodium percarbonate ($2Na_2CO_3 \bullet 3H_2O_2$)[5], and sulfate radical-based AOPs (peroxymonosulfate (PMS) and peroxydisulfate (PDS)[6]. The sulfate radical-based AOPs are particularly attractive due to their versatility in activation, which can be activated through various methods, including external energy (such as heat, electricity, ultraviolet light, and ultrasound, etc.), metal ions, and heterogeneous catalysts[7]. Compared with traditional hydroxyl radical-based AOPs (•OH: redox potential of 1.8-2.7 V vs. NHE and half-life of 20 ns), sulfate radical ($SO_4^{\bullet -}$: 2.5-3.1 V vs. NHE) [8]has longer life-span (30−40 μs), and a broader applicable pH range (pH=2-9). Besides, they exhibit high reactivity and oxidation capability toward a wide range of different types of micropollutants.

The first use of Co^{2+} to activate PMS for producing ROSs dates back to 1958, where it decomposed organic matter in water through sulfate radicals. Subsequent studies identified Co^{2+} as the most effective transition-metal activator for PMS[9]. This finding spurred the development of varied Co_3O_4-based materials. These materials have been shown to efficiently degrade organic

pollutants in water through radical-mediated pathways. An increasing number of Co-based catalysts such as Co_3O_4-MgO@C[10], $Co(OH)_2$/g-C_3N_4[11], MOF-derived Co_3O_4-C@FeOOH[12], Cu/Co_2P[13], and V_O-M-Co_3O_4@CNx[14] have been developed. Collectively, previous works have established crystal engineering as a powerful strategy for developing high-performance catalysts. For instance, Huanyan Xu have confirmed that the exposed (222) and (400) facets of Co_3O_4 readily adsorb PMS molecules and cleaved the O-O bond, thereby facilitating the charge transfer process[15]. Catalyst morphology also influences the selectivity of reactive oxygen species generation. Besides, Hexin Zhang and co-workers reported nanorod-like Co_3O_4 with (110) plane exposed exhibiting a superior activity for PMS activation to efficiently remove bisphenol A in water[16]. Huan Wang synthesized Co_3O_4 nanoparticles of different morphologies with predominantly exposed (001), (111), and (112) facets. This study systematically elucidates the influence of U-Co_3O_4 crystal facets on $^1O_2$ generation[17]. Therefore, facet-dependent ROSs generation behaviors have attracted more and more attentions.

In this work, we successfully synthesized ultra-dispersed hexagonal U-Co_3O_4 nanosheets with exposed (111) crystal facets with sacrificial template. The traditional nanosheets tend to aggregate, and specific crystal planes are difficult to be exposed. The waste fiber was used as templates to generate β-$Co(OH)_2$ nanosheet in situ. It was employed to fabricate ultra-dispersed Co_3O_4 nanosheet through calcining the β-$Co(OH)_2$ in the air atmosphere. The as-prepared ultra-dispersed Co_3O_4 with more exposed (111) facets can degrade 40 mg/L of 4-NiP within 10 min.

2. Experiment

2.1. Materials

Cobalt chloride hexahydrate ($CoCl_2·6H_2O$), polypropylene fiber, Hexamethylenetetramine (HMT), 4-nitrophenol (4-NiP), 2-Chloro-4-nitrophenol (2C4Nip), 2-Chloro-6-nitrophenol (2C6Nip), tetracycline (TC), p-nitrophenol (4-Nip), oxytetracycline (OTC), doxycycline hydrochloride (DOX), methylene blue (MB), methyl red (MR), methyl orange (MO), potassium peroxymonosulfate (PMS, $HSO_5·0.5KHSO_4·0.5K_2SO_4$), L-Histidine (L-His), isopropyl alcohol (IPA), ascorbic acid (VC), methyl alcohol (MeOH), and ethyl alcohol (EtOH) were purchased from Macklin reagent Co., Ltd. The used polypropylene fiber come from water filter cartridge.

2.2. Synthesis of Ultra-dispersed Co_3O_4 nanosheets

The Ultra-dispersed Co_3O_4 Nanosheet (U-Co_3O_4) was prepared as follow: In the typical procedure, used polypropylene fiber was cut into pieces, and washed many times. 360 mL water and 50 mL of ethanol were mixed in a beaker, then the polypropylene fiber was added. Subsequently, 2 mmol of $CoCl_2·6H_2O$ and 24 mmol of HMT were respectively dissolved in the above-mentioned mixed solution. The above mixture solution keep at 90 °C with stirring for 2 h. After the temperature of products dropped to room temperature, and washed with denonized water and ethanol for three times. Finally, The samples were treated by calcining (400, 500, and 600 °C) in the air atmosphere for 3 h. For comparison, Co_3O_4 sheet was prepared in the same procedure without polypropylene fiber.

2.3. Characterization techniques

The crystal structure of the catalysts was measured by a powder X-ray diffractometer (Rigaku Ultima IV, Japan) with Cu-Kα radiation. The microscopic morphology, lattice information, and elemental distribution of the samples were investigated by field emission scanning electron microscopy (FE-SEM, Carl Zeiss Bruker 6/30, Germany) and High-resolution transmission electron microscopy (HRTEM, JEM-2100, Japan). The chemical valence states of surface

elements were analyzed by X-ray photoelectron spectroscopy (XPS, ESCALAB-250Xi,USA) equipped with a monochromated Al Kα X-ray source (hv = 1486.6 eV), using a pass energy of 30 eV and a power of 100 W. The surface textural properties were analyzed with a multi-channel automatic surface area and porosity analyzer (Micromeritics TriStar II 3020, USA). The degradation process was monitored by UV–vis spectroscopy (P4, MAPADA, Shanghai).

2.4. Evaluation of catalytic performance

More specific analytical methods were presented in supporting information, see S 2.4.

2.5 *Computational details*

More DFT calculation could be found in the Supplementary Material, see S 2.5.

3. Results and discussion

3.1. XPS and XRD analysis

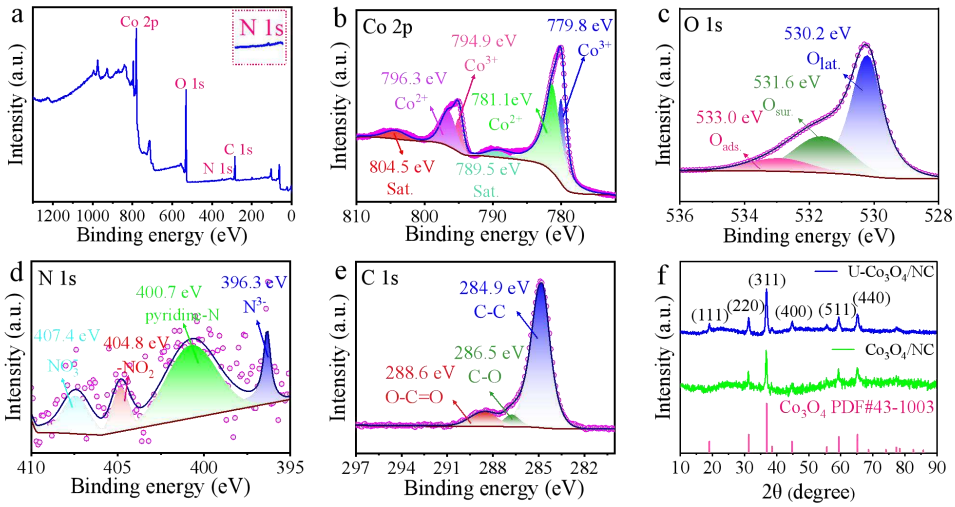


Fig. 1. XPS spectra of U-Co_3O_4/NC (a) full-survey spectrum; (b)Co 2p, (c) O1s, (d) N 1s, and (e) C 1s; (f) XRD patterns of samples.

The atomic composition and elemental valence states of U-Co_3O_4/NC was subsequently investigated by X-ray photoelectron spectroscopy (XPS) analysis. The samples exhibited signals corresponding to Co, O, N, and C elements(Fig. 1a).The four main peaks of $Co2p_{3/2}$ and $Co2p_{1/2}$ were observed (Fig. 1b). The two sharp characteristic peaks appeared at 781.1 and 794.9 eV were ascribed to Co^{2+}. Additionally, the peaks at 779.8 eV and 796.3 eV were assigned to Co^{3+}, confirming the presence of Co_3O_4 nanosheet[18]. The O 1s XPS spectra as shown in Fig. 1c, three kinds of peaks corresponded to surface adsorbed oxygen ($O_{ads.}$, 533.0 eV), chemisorbed oxygen ($O_{sur.}$, 531.6 eV), and lattice oxygen ($O_{lat.}$, 530.0 eV)[19,20]. In addition, the chemisorbed oxygen mainly includes the oxygen defects and some hydroxyl-like group. As depicted in Fig. 1d, the peak of pyridinic N was observed at 400.7 eV without graphitic N and oxidized N[21]. The pyridinic N can serve as an adsorption site to interact with PMS, thereby weakening the peroxide bond energy[22]. The XPS C 1s curve of U-Co_3O_4/NC could be fitted into three peaks at 288.6, 286.5, and 284.9 eV, which are assigned to O-C=O, C=O, and C-C (Fig. 1e). Moreover, this interaction alters the electronegativity of the adjacent carbon atom, generating Lewis base sites, which facilitated the transfer of numerous electrons from pyridinic N to PMS, leading to the production of $SO_4^{\bullet -}$. As shown in Fig. 1f, the X-ray diffraction (XRD) patterns of U-Co_3O_4/NC and Co_3O_4/NC are presented. All the observed diffraction peaks are consistent with previous reports and can be indexed to the spinel Co_3O_4 phase. Specifically, the characteristic peaks of

U-Co_3O_4/NC at 31.18°, 37.01°, 44.88°, 59.37°, and 65.31° correspond to the (111), (220), (311), (400), (511), and (440) crystal planes, respectively[23]. In comparison, the peak of (111) crystal planes were not observed, which may be attributed to the stacking of Co_3O_4 nanosheet in the absence of a fiber template.

3.2. SEM and TEM analysis

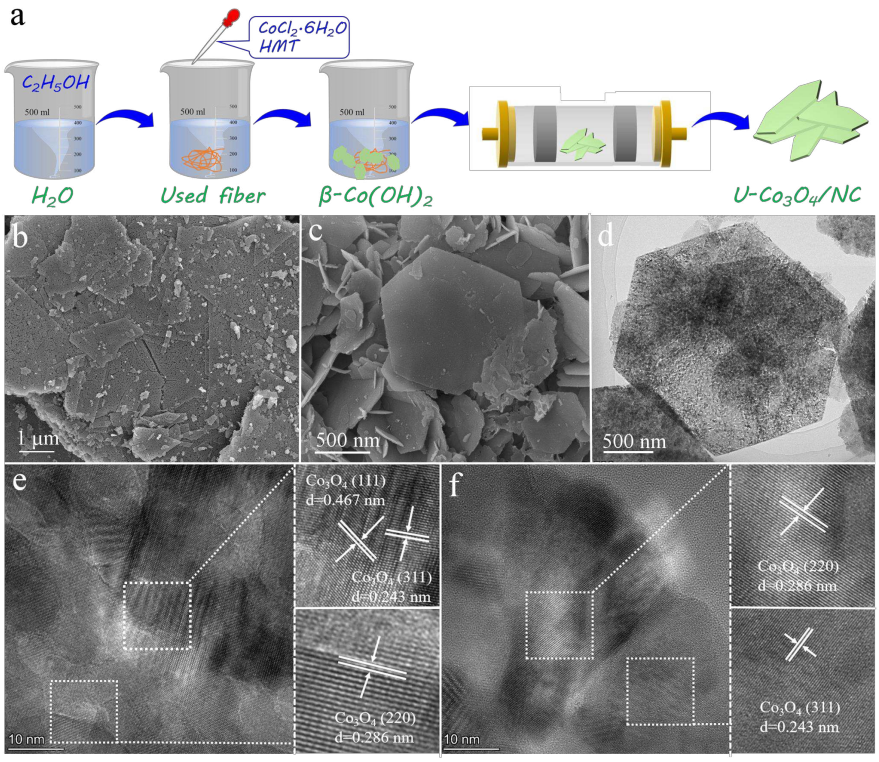


Fig. 2. (a) Synthetic schematic diagram of U-Co_3O_4; SEM images of (b) Co_3O_4/NC and U-Co_3O_4 (c); (d-f) TEM images of U-Co_3O_4/NC catalysts.

Fabrication of U-Co_3O_4/NC is depicted in Fig. 2a using waste fiber as a sacrificial template. The objective is to prepare highly dispersed Co_3O_4 nanosheets to enhance photocatalytic activity. For comparison, Co_3O_4/NC was prepared without template, it can be observed that Co_3O_4 nanosheets were stacked together (Fig. 2b). Noticeably, U-Co_3O_4/NC has a larger specific surface area of 39.43 m^2/g than Co_3O_4/NC (15.80 m^2/g), with a pore volume of 0.15 cm^3/g (Fig. 1S). Besides, the average pore size of U-Co_3O_4/NC (26.84 nm) was larger than Co_3O_4/NC (11.40 nm). The results indicated that U-Co_3O_4/NC nanosheets lead to mainly exposes more facets including (111). The (220) and (311) crystal planes of Co_3O_4/NC are observed in Fig. 2S, while the (111) plane is absent. The waste polypropylene fibers were shredded as a sacrificial template to prepare U-Co_3O_4/NC nanosheets (Fig. 2 c, d). The Co_3O_4 is arranged in a disordered nanoflower-like structure without stacking. The Co_3O_4 hexagonal nanosheets with the well-defined planes can be observed in Fig. 2e, Furthermore, the lattice spacing of Co_3O_4 was identified by HRTEM (Fig. 2 f), the crystal facets (111) (d= 0.467 nm), (311) (d=0.243 nm), and (220) (d=0.286 nm) of Co_3O_4 were observed, both of which were inconsistent with the data collected from the XRD spectrum.

3.3. Optimizing pyrolysis temperature, catalyst, and PMS dosage

The AOPs demonstrated remarkable performance in degrading emerging organic pollutants due to the variety of ROSs including $O_2^{\bullet -}$, $^1O_2$, •OH, and $SO_4^{\bullet -}$, which can rapidly react with pollutant molecules, breaking down organic matter and mineralizing it into carbon dioxide and water.[24].

The pyrolysis temperature is a main factor affecting the catalytic performance of U-Co_3O_4/NC. As shown in the Fig. 3a. 400 ℃ was confirmed as the optimal pyrolysis temperature through the 4-NiP degradation experiments using U-Co_3O_4/NC prepared under 400, 500, and 600 ℃, respectively. Effects of catalyst dosage and PMS concentration were evaluated[25]. As shown in Fig. 3b, the degradation efficiency improved significantly when the dosage of U-Co_3O_4/NC was increased from 10 mg to 20 mg, which can be attributed to enhance ROSs production. However, a further increase to 30 mg resulted in no significant change in the degradation rate. This phenomenon can be explained by the excessive catalyst causing strong adsorption of ROSs. Regarding PMS concentration, values of 0.5, 1.0, and 1.5 mmol were evaluated. Clearly, 1.0 mmol of PMS was sufficient for the degradation of 4-NiP(Fig. 3c). Series of control experiments were conducted to assess the 4-NiP degradation activity of U-Co_3O_4/NC and Co_3O_4/NC in the presence of PMS and simulated sunlight. The results indicated that U-Co_3O_4/NC did not decompose the 4-NiP(Fig. 3d). Additionally, simulated sunlight can drive efficiently PMS activation for 4-NiP degradation.

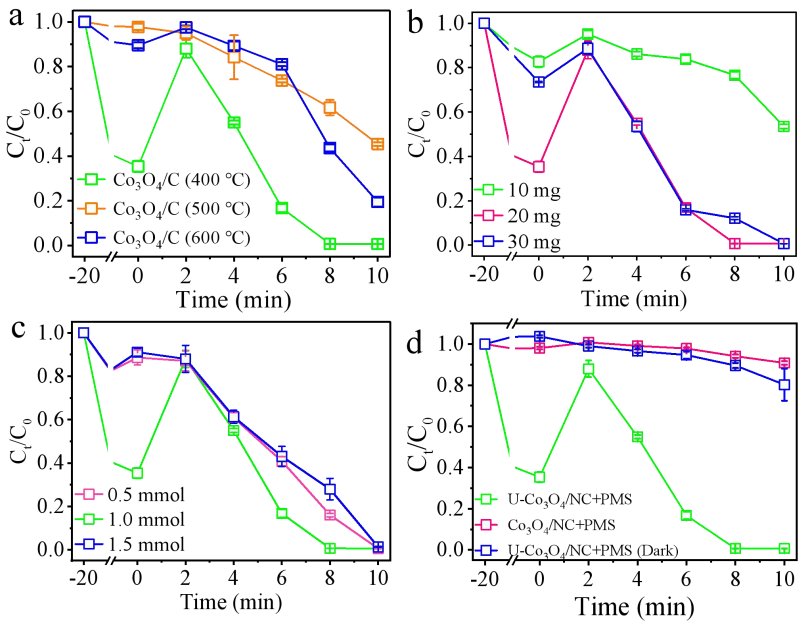


Fig. 3. Effects of pyrolysis temperature(a), catalyst dosage(b), and PMS concentration(c) on 4-NiP degradation; The effect of light on 4-NiP degradation(d).

3.4. Effect of pH

The effect of pH on 4-NiP degradation was illustrated in Fig. 4a. It is worth noting that pH affects both the ionization state of the pollutant and the surface-charge properties of the catalyst, which alters catalyst-reactant interactions, subsequently affecting the reaction direction, rate, and the ROSs generated. The highest degradation efficiency in PMS-activated Fenton-like processes was commonly observed within pH 2.0-10.0, which was attributable to the potent oxidizing capacity of $SO_4^{\bullet-}$. Above pH 10.0, however, the conversion of $SO_4^{\bullet-}$ to •OH diminished degradation efficiency significantly[26,27]. We specifically paid more attention to the 4-NiP degradation under alkaline conditions, observing an accelerated rate compared to neutral pH. Therefore, U-Co_3O_4/NC displayed high tolerance toward the pH values.

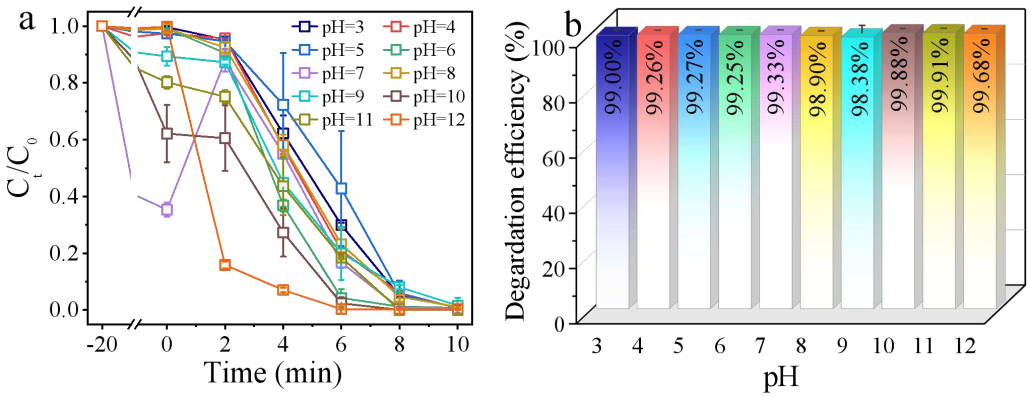


Fig. 4. (a) The degradation of 4-NiP in different initial pH value solutions, (b) the degradation efficiency of 4-NiP.

3.5. Influence of the co-existing ions

There is an undeniable fact that the coexistence of anions in the actual wastewater have negative impact on the PMS involved process. The environmental adaption of U-Co_3O_4/NC catalysts was evaluated in the presence of various inorganic anions. Herein, we have investigated the effect of typical anions (1 mmol of HCO_3^-, Cl^-, SO_4^{2-}, $H_2PO_4^-$, HPO_4^{2-}, and NO_3^-) on the degradation performance in Fig. 5. In general, HCO_3^- and NO_3^- have a significant influence on 4-NiP degradation, which maybe because the HCO_3^- and NO_3^- can consume lots of $SO_4^{\bullet -}$ and •OH in the AOPs (Eqs. 1-4)[28]. Moreover, the slight inhibition effect of Cl^- and SO_4^{2-} was observed since they can react with the ROSs (such as $SO_4^{\bullet -}$ and •OH) to generate other species with lower redox potential or quench these radicals (Eqs. 5-6)[29]. In contrast, HPO_4^{2-} has notably enhanced the degradation efficiency of 4-NiP, which was conducive to further generation of the other ROSs (Eqs. 7-10)[30]. Therefore, the increase of degradation efficiency of 4-NiP with the addition of $H_2PO_4^-$, HPO_4^{2-} was more obvious.

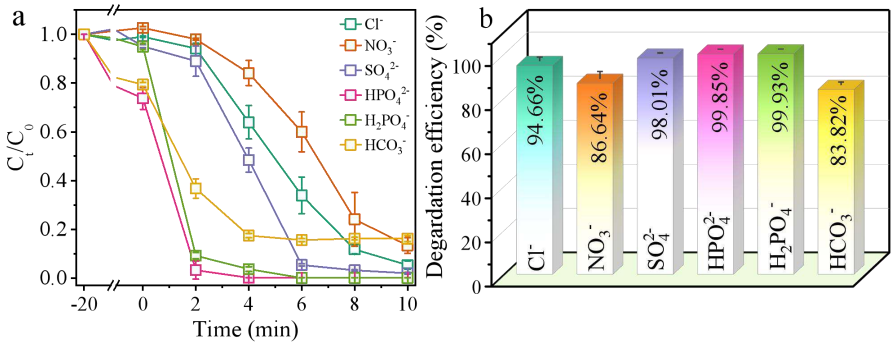


Fig. 5. Effects of (a) anion on 4-NiP degradation, (b) and the removal efficiency of 4-NiP.

$$SO_4^{\bullet -} + HCO_3^- \rightarrow SO_4^{2-} + HCO_3^{\bullet} \quad (1)$$

$$\bullet OH + HCO_3^- \rightarrow CO_3^{\bullet -} + H_2O \quad (2)$$

$$SO_4^{\bullet -} + NO_3^- \rightarrow NO_3^{\bullet} + SO_4^{2-} \quad (3)$$

$$\bullet OH + NO_3^- \rightarrow NO_3^{\bullet} + OH^- \quad (4)$$

$$Cl^- + SO_4^{\bullet -} \rightarrow SO_4^{2-} + Cl^{\bullet} \quad (5)$$

$$Cl^- + \bullet OH \rightarrow OH^- + Cl^{\bullet} \quad (6)$$

$$SO_4^{\bullet -} + H_2PO_4^- \rightarrow H_2PO_4^{\bullet -} + SO_4^{2-} \quad (7)$$

$$\bullet OH + H_2PO_4^{2-} \rightarrow H_2PO_4^{\bullet -} + OH^- \quad (8)$$

$$SO_4^{\bullet -} + HPO_4^- \rightarrow HPO_4^{\bullet} + {}^-SO_2^{2-} \quad (9)$$

$$\bullet OH + HPO_4^- \rightarrow HPO_4^{\bullet -} + OH^- \quad (10)$$

3.6. Reusability and generality

In practical applications, generality and reusability are the most significant parameters for catalytic materials[31,32]. The universality of the catalyst U-Co_3O_4/NC was applied to the catalytic degradation under different light irradiation. As shown in Fig.6 a, Co_3O_4/NC can still completely reduce the 4-NiP within 10 min under Xe light and sunlight. Besides, investigation was conducted in simulated kinds of actual water bodies such as deionized water (De-W), tap water (Ta-W), river water (Ri-W), and reservoir water (Re-W). The U-Co_3O_4/NC/PMS system achieved a removal efficiency of 99.99% for 4-NiP in Ta-W, Ri-W, and Re-W, respectively (Fig. 6 b). These results revealed that the inhibitory effect of matrices on 4-NiP degradation was unobvious. Thus, U-Co_3O_4/NC had a certain anti-interference ability for natural water. U-Co_3O_4/NC can still completely degrade the 4-NiP within 10 min for 5 successive cycles, and the conversion at 10 min in the 5th run is 96.86% (Fig.6 c), exhibiting good reusability. However, industrial wastewater typically contains 4-NiP at high concentrations, generally above 2 g/L. In this work, the concentration of 4-NP degraded is the highest reported in the literature (Table 1).

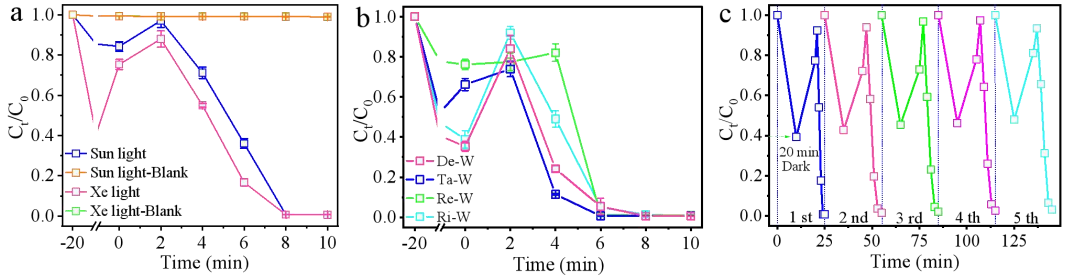


Fig. 6. Effects of light irradiation (a) and different water matrices (b) on the 4-NiP degradation; The recyclability of the catalyst (c).

Broader applicability for removal of other organic pollutants was depicted in Fig.7. 40 mg/L of 4-nitrophenol (4-NiP), 2-Chloro-4-nitrophenol (2C4Nip), 2-Chloro-6-nitrophenol (2C6Nip), tetracycline (TC), doxycycline (DOX), methyl orange (MO), oxytetracycline (OTC), methylene blue (MB), and methyl red (MR) were selected as target pollutants. The specific removal rate of target pollutants was provided in the Table 1S. The efficiency of target pollutants was higher than 95% except for TC and DOX in river water matrices. The mixture of antibiotics (OTC, TC, and DOX, (Fig. 7b)), phenols (4-NiP, 2C4Nip, and 2C6Nip)(Fig.7c)), and dyes (MO, MR, and MB) (Fig.7d)) were decomposed by U-Co_3O_4/NC/PMS within 10 min in natural water, and the mixture was almost mineralized according to the ultraviolet-visible spectrum[33,34].

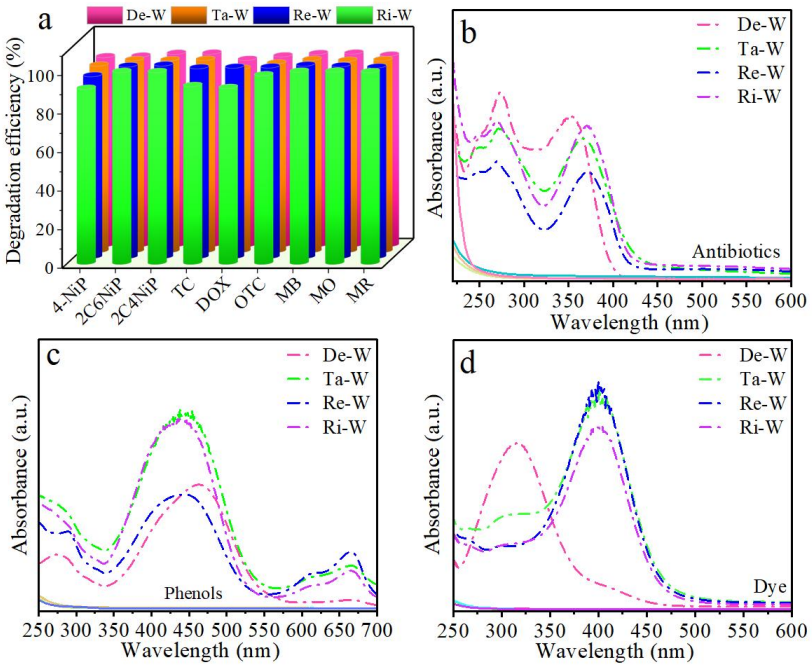


Fig. 7. (a) Effects of different water matrices on nine kinds of organic pollutants degradation; The degradation efficiency of mixture of antibiotics (b), phenols (c), and dyes (d) by U-Co_3O_4/NC/PMS in different water matrices.

Table 1. The degradation of 4-NiP recently published.

Catalyst	BET $m^2.g^{-1}$	P. Conc.	Time (min)	Drive force	D (%)	Cycle time	Ref.
Ca-AIS	65.170	15 mg/L	120	Vis-L	63.2	–	[35]
45CMO/CN-Nv	96.9	5 ppm	15	Vis-L	100	5	[36]
ZnONPs	–	20 mg/L	180	Uv-L	92	–	[37]
CoO- Fe_2O_3@SiO_2@TiO	–	20 µg/L	240	Vis-L	98.3	–	[38]
Fe_1/C-CN	94.4	10 mg/L	90	Vis-L	99.3	5	[39]
CuO-II	–	10 mg/L	10	Vis-L	100	10	[40]
U-Co_3O_4/NC	39.43	40 mg/L	6	Vis-L	99.99	5	This work

P. Conc., Pollutants Concentration; D, Degradation rate; Ref., reference; BET, Bruner-Emmet-Teller; Vis-L, Visible light; Uv-L, ultraviolet light;-, No report; AIS, doped $AgInS_2$; NPs, nanoparticles; CMO/CN-Nv, nitrogen vacancies composite with $CoMoO_4$;CN,g_3N_4; CuO-II, calcination temperature for 350°C.

3.7. Degradation mechanism

3.7.1. The free radical trapping experiments

The ROSs in the U-Co_3O_4/NC/PMS system was evaluated by radical trapping experiment using various scavengers, where MeOH, IPA, L-His, and VC were used to selectively quench •OH/$SO_4^{\bullet -}$, •OH, $^1O_2$, and $O_2^{\bullet -}$, respectively[41]. As depicted in Fig. 8 a, the degradation efficiency of blank solution is 99.0% within 10 min. When 0.5, 1.0 and 3.0 mmol of MeOH are added into the system, the degradation efficiency decreased to 47.4 % sharply[42]. The results indicated that the high yields of •OH and $SO_4^{\bullet -}$. Meanwhile, the removal of 4-Nip decreased from 99.8% to 66.9%, 46.9%, and 33.2%, after adding 0.3, 0.6, 1.0 mmol of IPA, respectively. As shown in Fig. 8 b, tiny IPA had strong inhibitory effect on the degradation of 4-Nip, indicating that the •OH had obvious effect on 4-Nip degradation. L-Histidine (L-His) was used as a quenching agent for $^1O_2$[43]. When 0.0005, 0.001, 0.002 mmol of L-His was added, the degradation efficiency of 4-Nip decreased

after 10 min of reaction, indicating that tiny quenching agent had remarkable effect on 4-Nip degradation (Fig. 8 c)[44]. The same phenomenon was also observed in Fig.8 d, the removal efficiency of 4-Nip dropped to 0.5 % when 0.3 mmol of VC was added, these results suggested that $^1O_2$, and $O_2^{\bullet -}$ had inhibitory effect on 4-Nip degradation. These results confirmed that $SO_4^{\bullet -}$, $^1O_2$, $O_2^{\bullet -}$, and •OH were the main ROSs to degrade 4-Nip.

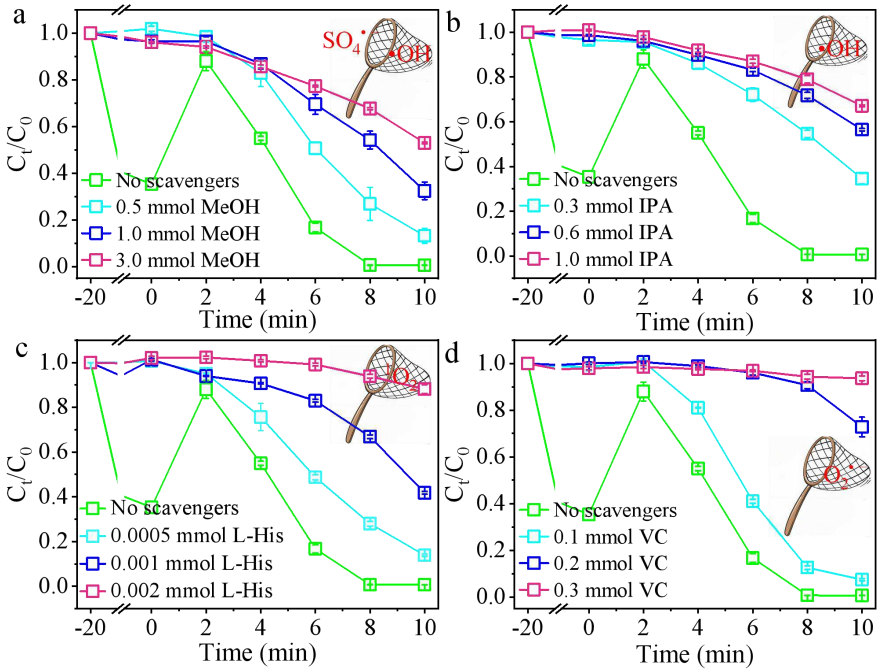


Fig. 8. The inhibitory effect of (a) MeOH, (b) IPA, (c) L-His, and (d) VC on 4-NiP removal efficiency.

3.7.2. EPR investigation

PMS-based Fenton-like process by catalytic activation of PMS included the free radicals ($SO_4^{\bullet -}$, •OH, and $O_2^{\bullet -}$) and non-radical ($^1O_2$) pathways. The generated ROSs were verified by EPR, for identifying the ROSs in the U-Co_3O_4/NC/PMS system, EPR experiments can effectively monitors the superoxide radicals ($O_2^{\bullet -}$), sulfate radicals ($SO_4^{\bullet -}$), and hydroxyl radicals (•OH) using 5, 5-dimethyl-1-pyrroline-N-oxide (DMPO), as well as singlet oxygen ($^1O_2$) using 2, 2, 6, 6-tetramethylpiperidine (TEMP) as capture reagent. EPR signals corresponding to DMPO-•OH, DMPO-$SO_4^{\bullet -}$ were observed in dark condition, and the intensity of signals under irradiation became stronger than that in dark condition. The above results indicated that $SO_4^{\bullet -}$ and •OH served as the primary ROSs in the non-radical pathway for 4-NiP degradation[45]. The signals of DMPO-$O_2^{\bullet -}$ radicals were captured, the intensity was increased after light irradiation (Fig. 8 b), indicating enhanced PMS activation by U-Co_3O_4/NC under light synergy exhibited much stronger EPR signal intensity. Under dark condition, TEMP-h^+ radicals were detected in U-Co_3O_4/NC/PMS, the signal intensity became weaker than that under light irradiation, explaining its significant contribution in the 4-NiP degradation progress. The intensity of TEMP-$^1O_2$ was stronger at 2 min than that in dark condition[46]. Therefore, these results indicated the fact that electrons photogenerated by light irradiation can accelerate PMS activation and generate $SO_4^{\bullet -}$, $^1O_2$, and •OH. A possible mechanism of PMS activation over U-Co_3O_4/NC was proposed based on the above analysis. The ions of Co^{2+} and Co^{3+} can activate PMS generating $SO_5^{\bullet -}$ and $SO_4^{\bullet -}$. In addition, Co^{2+}/Co^{3+} can be regenerated by photo-induced electron to finish the redox cycle (Eqs. (13)), which kept the U-Co_3O_4/NC sample to work continuously. The ROSs of $O_2^{\bullet -}$ was produced

as following Eqs. (14)–(16)[47]. Moreover, in this process, $^1O_2$ can be formed through a series of reaction such as (Eqs. (17) and (21)). Therefore, 4-NiP can be degraded by the •OH, $SO_4^{\bullet -}$,$^1O_2$, and $O_2^{\bullet -}$ as radical and non-radical pathway, and be decomposed into CO_2, H_2O and small molecular products (Eqs. (22)). To further investigate the influence of different Co_3O_4 facets, Density Functional Theory (DFT) calculations were performed. The crystal planes were chosen for theoretical study on the basis of their relatively high-intensity signals in the XRD pattern. The results suggest that during the activation process, Co atoms can coordinate with the O-O group of PMS, which is oriented perpendicular to the 2D plane of U-Co_3O_4. The adsorption energies (E_{ads}) for PMS binding via its O-O group on the (111), (220), and (331) facets were calculated to be -3.93, -3.98, and -3.25 eV, respectively. Among them, the (111) and (220) facet exhibits the stronger adsorption energy, indicating its strong binding with PMS and confirming it as the primary active site. Therefore, the adsorption model where the (111) facet adsorbed the O-O site of the PMS played important role on catalytic performance.

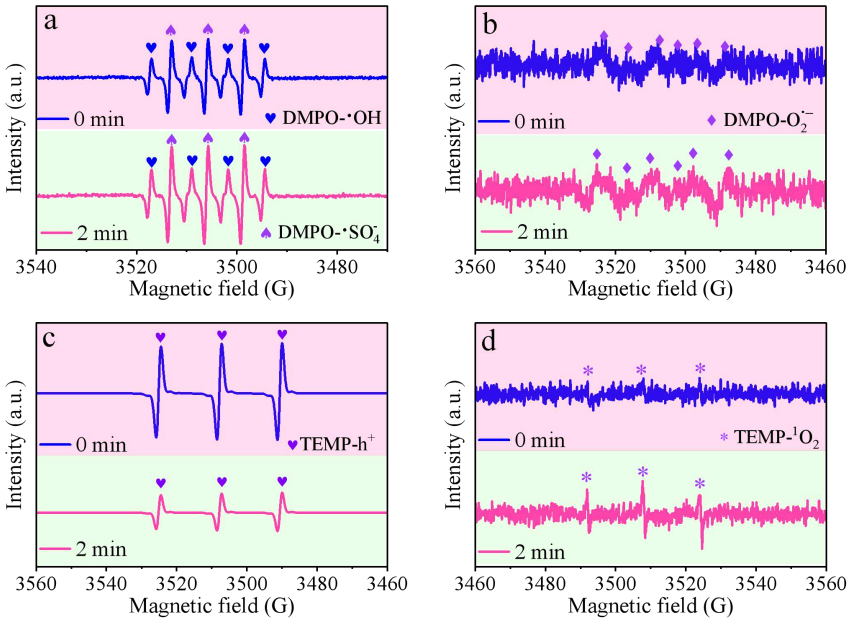


Fig. 9. EPR spectra of (a) •OH and $SO_4^{\bullet -}$, (b) $O_2^{\bullet -}$, (c) h^+, and (d)$^1O_2$.

$$Co^{2+} + HSO_5^- + H^+ \rightarrow H_2O + SO_4^{\bullet -} + Co^{3+} \quad (11)$$

$$Co^{3+} + HSO_5^- \rightarrow H^+ + SO_5^{\bullet -} + Co^{2+} \quad (12)$$

$$Co^{3+} + e^- \rightarrow Co^{2+} \quad (13)$$

$$SO_4^{\bullet -} + H_2O \rightarrow SO_4^{2-} + \bullet OH \quad (14)$$

$$H_2O_2 + \bullet OH \rightarrow HO_2^{\bullet} + H_2O \quad (15)$$

$$HO_2^{\bullet} \rightarrow H^+ + O_2^{\bullet -} \quad (16)$$

$$HO_2^{\bullet} + \bullet OH \rightarrow {}^1O_2 + H_2O \quad (17)$$

$$HO_2^{\bullet} + SO_4^{\bullet -} \rightarrow {}^1O_2 + HSO_5^- \quad (18)$$

$$O_2^{\bullet -} + O_2^{\bullet -} + 2H^+ \rightarrow {}^1O_2 + H_2O_2 \quad (19)$$

$$O_2^{\bullet -} + \bullet OH + 2H^+ \rightarrow \bullet OH + {}^1O_2 \quad (20)$$

$$HSO_5^- + SO_5^{2-} \rightarrow HSO_4^- + SO_4^{2-} + {}^1O_2 \quad (21)$$

$$O_2^{\bullet -}/{}^1O_2/\bullet OH + \text{pollutant} \rightarrow \text{Degradation Products} + CO_2 + H_2O + SO_3 \quad (22)$$

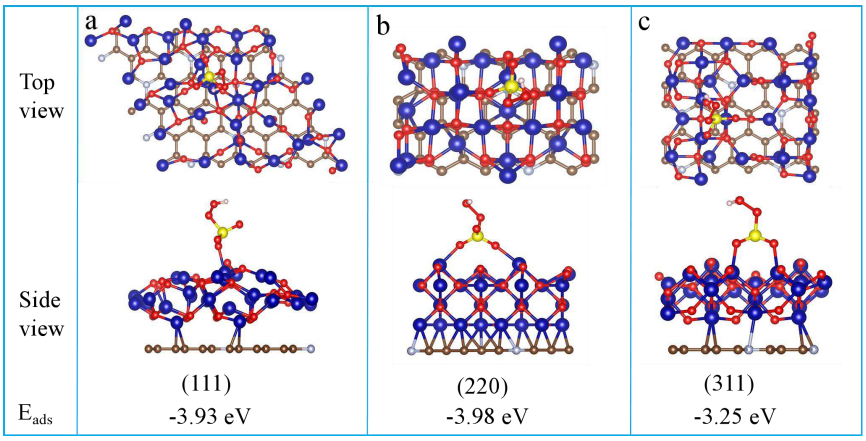


Fig. 10. The E_{ads} of PMS's O-O bind adsorbed on the U-Co_3O_4 facet (a) (111), (b) (220) and (c) (311).

3.7.3. Pathway and toxicity analysis

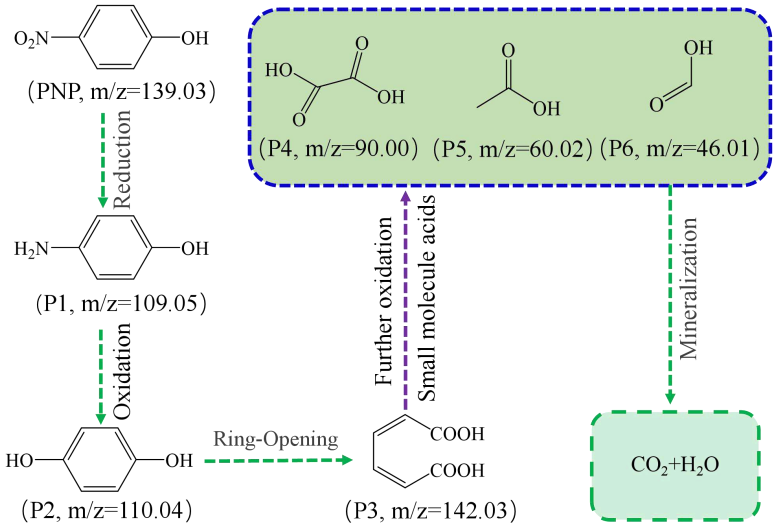


Fig. 11. Possible degradation pathways of 4-NiP in U-Co_3O_4/NC/PMS.

The intermediates products of 4-NiP degradation were identified and distinguished by LC–MS, and the possible degradation pathways were depicted in Fig. 11. The hydroxylation, oxidation reaction and fracture of C=C bonds were the major degradation mechanisms. From the Fig. 11, it can be inferred that P1 (m/z = 109) and P2 (m/z = 110) were obtained from the nitro reduction, and the hydroxylation of 4-NiP, respectively. Electron-donating groups, including hydroxyl and amido groups, can be easily oxidized by an electron transfer mechanism. Moreover, P3 (m/z = 142) was produced by oxidative ring opening[48]. P3 was further oxidated by free radicals to form P4 (m/z = 90), P5 (m/z = 60), and P6 (m/z = 46). The intermediates were subsequently decomposed to smaller intermediates (not detected) and mineralized into CO_2 and H_2O.

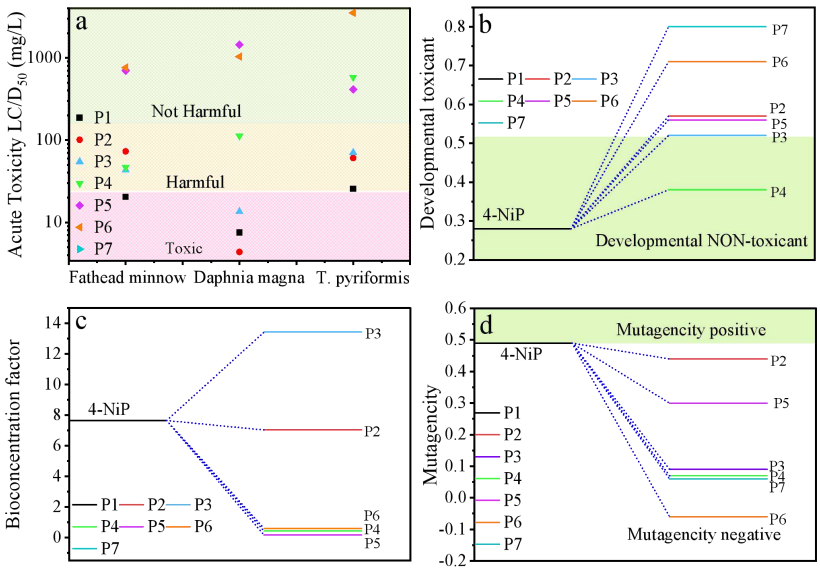


Fig. 12. (a) Acute and chronic toxicity, (b) Developmental toxicity, (c) Bioaccumulation factor, and (d) Mutagenicity of 4-NiP and its degradation intermediates.

Furthermore, the acute toxicity LC/D50, bioaccumulation factor, mutagenicity and developmental toxicity of 4-NiP were evaluated using Toxicity Estimation Software Tool (T. E. S. T.), evaluating aspects such as toxicity, developmental toxicity, mutagenicity and bioaccumulation concentrations. Toxicity assessments utilizing fathead minnow, daphnia magna and Ptriformis as model species demonstrated a progressive decline in the toxicity of the intermediate products generated during 4-NiP degradation (Fig. 12a). Developmental toxicity evaluations showed that nearly all intermediate products exhibited developmental toxicity, primarily due to the presence of benzene rings, which inherently influence their toxicological profiles (Fig. 12b)[49,50]. In terms of bioaccumulation analysis, nearly all intermediate products except P3, exhibited a progressive decline in the toxicity of the intermediate (Fig. 12c). Notably, most intermediate products demonstrated lower mutagenicity compared to 4-NiP itself, the overall trend of degradation process showed a reduction in the bioaccumulation (Fig. 12d). These findings indicated that the intermediates of 4-NiP possess markedly reduced toxicity compared to 4-NiP.

4. Conclusion

Co_3O_4 nanosheets tend to agglomerate due to the van der Waals forces, leading to difficulties in dispersion, which has become a bottleneck in their applications in wastewater treatment. To address the dispersion issue of Co_3O_4 nanosheet, prepared it in-situ growth on waste fibers as sacrificial molds, and pyrolysis generating U-Co_3O_4/NC nanosheets. 40 mg/L of 4-NiP can be degraded by U-Co_3O_4/NC nanosheet within 10 minutes across a broad pH range of 2.0–10.0. Moreover, U-Co_3O_4 nanosheets are capable of degrading various 40 mg/L pollutants within 10 min, including 4-nitrophenol (4-NiP), 2-chloro-4-nitrophenol (2C4NiP), 2-chloro-6-nitrophenol (2C6NiP), tetracycline (TC), doxycycline (DOX), methyl orange (MO), oxytetracycline (OTC), methylene blue (MB), and methyl red (MR). The (111) facet of U-Co_3O_4/NC exhibits the stronger adsorption energy with PMS and confirming it as the primary active site. The mechanism of 4-NiP degradation demonstrated that the •OH, $SO_4^{\bullet -}$, $^1O_2$, and $O_2^{\bullet -}$as radical and non-radical pathway, and it was decomposed into CO_2, H_2O and small molecular products. This work presents a new strategy for fabricating U-Co_3O_4/NC nanosheet via a sacrificial template method, offering a promising approach for wastewater treatment.

Acknowledgments

This work was supported by the Science and Technology Plan Project of Guyuan City (2025GKJYF0015), the Ningxia Natural Science Foundation Project (2025AAC030606), the Key Laboratory of Green Catalytic Materials and Technology of Ningxia Province' project (2025SYSZD-03), and the Research Project Funding for Higher Education Institutions in Ningxia (NXG2024183).

Data availability statement

Data supporting the findings of this study are available from the corresponding author upon reasonable request.

Declarations

Competing interests The authors declare that they have no known competing financial interests or personal relationships that could have appeared to influence the work reported in this paper.

Ethical Approval Not applicable.

References

[1] L. A. Bermúdez, J. M. Pascual, M. D. M. M. Martínez, J. M. Poyatos Capilla, Effectiveness of advanced oxidation processes in wastewater treatment: state of the art, Water. 13 (2021) 2094.

[2] X. Chen, W. Fu, Z. Yang, Y. Yang, Y. Li, H. Huang, X. Zhang, B. Pan, Enhanced H_2O_2 utilization efficiency in Fenton-like system for degradation of emerging contaminants: oxygen vacancy-mediated activation of O_2, Water Res. 230 (2023) 119562.

[3] J. Du, C. Wang, M. Sun, G. Chen, C. Liu, X. Deng, R. Chen, Z. Zhao, Novel vacuum UV/ozone/peroxymonosulfate process for efficient degradation of levofloxacin: performance evaluation and mechanism insight, J. Hazard. Mater. 463 (2024) 132916.

[4] B. Liu, W. Guo, W. Jia, H. Wang, S. Zheng, Q. Si, Q. Zhao, H. Luo, J. Jiang, N. Ren, Insights into the oxidation of organic contaminants by Co(II) activated peracetic acid: the overlooked role of high-valent cobalt-oxo species, Water Res. 201 (2021) 117313.

[5] J. Gao, R.F. Nunes, K. O'Shea, G. L. Saylor, L. Bu, Y. Kang, X. Duan, D. D. Dionysiou, S. Luo, UV/Sodium percarbonate for bisphenol a treatment in water: Impact of water quality parameters on the formation of reactive radicals, Water Res. 219 (2022) 118457.

[6] G. Zhou, R. Zhou, Y. Liu, L. Zhang, L. Zhang, Y. Fu, Efficient degradation of sulfamethoxazole using peracetic acid activated by zero-valent cobalt, J. Environ. Chem. Eng. 10 (2022) 107783.

[7] B. Li, Y. Wang, L. Zhang, H. Xu, Enhancement strategies for efficient activation of persulfate by heterogeneous cobalt-containing catalysts: a review, Chemosphere. 291 (2022) 132954.

[8] J. Miao, Y. Jiang, X. Wang, X. Li, Y. Zhu, Z. Shao, M. Long, Correlating active sites and oxidative species in single-atom catalyzed Fenton-like reactions, Chem. Sci. 15 (2024) 11699–11718.

[9] X. Zhao, Z. Zhang, Heterogeneous peroxymonosulfate-based advanced oxidation mechanisms: new wine in old bottles? Environ. Sci. Technol. 59 (2025) 5913–5924.

[10] L. Chang, X. Xue, Q. Deng, X. Xie, X. Zhang, C. Cheng, H. Chai, Y. Huang, Modulating the electronic structure of Co center via MgO@C co-doping for PMS activation to remove levofloxacin, Sep. Purif. Technol. 321 (2023) 124151.

[11] S. Mao, P. Zhao, Y. Wu, C. Liu, M. Xia, F. Wang, Promoting charge migration of

$Co(OH)_2$/g-C_3N_4 by hydroxylation for improved PMS activation: catalyst design, DFT calculation and mechanism analysis, Chem. Eng. J. 451 (2023) 138503.

[12] H. Chen, J. Wang, MOF-derived Co_3O_4-C@FeOOH as an efficient catalyst for catalytic ozonation of norfloxacin, J. Hazard. Mater. 403 (2021) 123697.

[13] Y. Dong, G. Chen, X. Zuo, J. Li, J. Yu, G. Zhang, J. Kuang, I. Akpinar, L. Peng, X. Tang, J. Dong, L. Lin, P. Lyu, S. Yang, J. Li, Nitrogen, sulfur Co-doped hollow carbon-encapsulated Cu/Co_2P for selective oxidation esterification of furfurals, ACS Catal. 14 (2024) 6565–6576.

[14] R. Su, Y. Gao, L. Chen, Y. Chen, N. Li, W. Liu, B. Gao, Q. Li, Utilizing the oxygen-atom trapping effect of Co_3O_4 with oxygen vacancies to promote chlorite activation for water decontamination, Proc. Natl. Acad. Sci. U. S. A. 121 (2024) e2319427121.

[15] B. Li, H. Xu, Y. Liu, Y. Liu, Y. Xu, S. Zhang, Unveiling the structure–activity relationships of ofloxacin degradation by Co_3O_4-activated peroxymonosulfate: from microstructures to exposed facets, Chem. Eng. J. 467 (2023) 143396.

[16] L. Zhao, J. Zhang, Z. Zhang, T. Wei, J. Wang, J. Ma, Y. Ren, H. Zhang, Co_3O_4 crystal plane regulation to efficiently activate peroxymonosulfate in water: the role of oxygen vacancies, J. Colloid Interface Sci. 623 (2022) 520–531.

[17] H. Wang, D. Wang, C. Sun, X. Zhao, C. Xu, Z. Li, Y. Hou, L. Lei, B. Yang, X. Duan, Oriented generation of $^1O_2$ from peroxymonosulfate via Co_3O_4 facet engineering, App. Catal. B: Environ. 364 (2025) 124854.

[18] R. Liu, Y. Chu, Y. Li, K. Li, T. Li, H. Yu, R. Liang, Y. Chen, T. Wu, H. Yin, Facet effect on nanosheet Co_3O_4 catalysts for toluene oxidation: decisive role of Co^{3+} and reaction-induced oxygen vacancy, J. Environ. Chem. Eng. 12 (2024) 112640.

[19] Y. Pang, X. Zhou, E. I. Vovk, C. Guan, S. Li, A. P. Van Bavel, Y. Yang, Understanding lanthanum oxide surface structure by DFT simulation of oxygen 1s calibrated binding energy in XPS after in situ treatment, Appl. Surf. Sci. 548 (2021) 149214.

[20] U. J. Etim, P. Bai, O. M. Gazit, Z. Zhong, Low-temperature heterogeneous oxidation catalysis and molecular oxygen activation, Catal. Rev. 65 (2023) 239–425.

[21] P. Lazar, R. Mach, M. Otyepka, Spectroscopic fingerprints of graphitic, pyrrolic, pyridinic, and chemisorbed nitrogen in N-doped graphene, J. Phys. Chem. C. 123 (2019) 10695–10702.

[22] J. Gu, H. Wang, S. Li, M. Sohail Riaz, J. Ning, X. Pu, Y. Hu, Tuning pyridinic-N and graphitic-N doping with 4, 4′-bipyridine in honeycomb-like porous carbon and distinct electrochemical roles in aqueous and ionic liquid gel electrolytes for symmetric supercapacitors, J. Colloid Interface Sci. 635 (2023) 254–264.

[23] P. Tharasan, M. Somprasong, N. Kenyota, N. Kanjana, W. Maiaugree, W. Jareonboon, P. Laokul, Preparation and electrochemical performance of nanostructured Co_3O_4 particles, J. Nanopart. Res. 24 (2022) 126.

[24] C. Kuang, G. Zeng, Y. Zhou, Y. Wu, D. Li, Y. Wang, C. Li, Integrating anodic sulfate activation with cathodic H_2O_2 production/activation to generate the sulfate and hydroxyl radicals for the degradation of emerging organic contaminants, Water Res. 229 (2023) 119464.

[25] S. Wang, J. Wang, Synergistic effect of PMS activation by Fe^0@Fe_3O_4 anchored on N, S, O co-doped carbon composite for degradation of sulfamethoxazole, Chem. Eng. J. 427 (2022) 131960.

[26] Z. Liu, W. Hao, C. Yuan, W. Ruan, W. Jiang, F. Teng, Substantially updating photocatalytic

reaction by in-situ generated SO_4^- through directly exciting SO_4^{2-}, Water Process. Eng. 48 (2022) 102912.

[27] B. Wu, S. Wu, L. Hu, A simple fabrication of pH-modified $BiVO_4$ to enhance the degradation of tetracycline by peroxymonosulfate activation under simulated sunlight, J. Environ. Chem. Eng.13 (2025) 115320.

[28] L. Li, M. Cheng, H. Sun, H. Yi, S. Liu, M. Zhang, Y. Fu, X. Zhou, F. Xu, D. Ma, G. Zeng, Z. Yang, C. Lai, Assessing the discrepant role of anions in the transformation of reactive oxygen species in H_2O_2 and PDS system: a comparative kinetic analysis, J. Hazard. Mater. 480 (2024) 136465.

[29] N. Ahmed, D. Vione, L. Rivoira, L. Carena, M. Castiglioni, M. C. Bruzzoniti, A review on the degradation of pollutants by Fenton-like systems based on zero-valent iron and persulfate: effects of reduction potentials, pH, and anions occurring in waste waters, Molecules. 26 (2021) 4584.

[30] N. Wu, R. Qu, C. Li, M. Bin-Jumah, A. A. Allam, W. Cao, Y. Yu, C. Sun, Z. Wang, Enhanced oxidative degradation of decabromodiphenyl ether in soil by coupling Fenton-persulfate processes: insights into degradation products and reaction mechanisms, Sci. Total Environ. 737 (2020) 139777.

[31] F. Gao, Z. Xiong, Y. Jia, H. Li, J. Li, Cu-boosted one-pot nanoarchitectonics for synthesis of polydopamine membranes as reusable laccase mimic, J. Colloid Interface Sci. 628 (2022) 935–942.

[32] M. Yoon, H. Jeon, J. Park, J. Jang, H. Choi, J. Kim, D. Kim, K. Shim, T. Park, G. Kwon, J. Kim, Facile fabrication of MOF and natural polymer-derived carbon-aerogels with multiscale porosity for persulfate activation in water treatment, J. Mater. Chem. A. 13 (2025) 26350–26363.

[33] W. Jiang, J. Yang, Y. Wang, Y. Gao, W. Ren, Y. Yu, Q. Liu, Efficient dye degradation via Fenton-like catalysis using GO/MX-Fe^{2+} composites: synthesis, performance, and mechanism, Water Process. Eng. 77 (2025) 108422.

[34] Y. Li, C. Zhang, G. Zhao, Z. Zhang, P. Su, Y. Li, Y. Mu, W. Zhou, A critical review on the activation of peroxymonosulfate by MOFs for antibiotics degradation: affecting factor, performance and mechanism, J. Environ. Chem. Eng. 12 (2024) 113634.

[35] X. Wang, S. Liu, S. Lin, K. Qi, Y. Yan, Y. Ma, Visible light motivated the photocatalytic degradation of p-nitrophenol by Ca^{2+}-doped $AgInS_2$, Molecules. 29 (2024) 361.

[36] Q. Zhu, Q. Shi, Y. Hou, Y. Hao, Interface engineered s-scheme $CoMoO_4$/CN heterojunctions with n-vacancy modulation: photogenerated hole-dominated nonradical pathways in PMS-activated photocatalysis, J. Colloid Interface Sci. 700 (2025) 138421.

[37] Y. Wang, C. Yang, Y. Liu, Y. Fan, F. Dang, Y. Qiu, H. Zhou, W. Wang, Y. Liu, Solvothermal synthesis of ZnO nanoparticles for photocatalytic degradation of methyl orange and p-nitrophenol, Water. 13 (2021) 3224.

[38] S. M. Sajjadi, Z. Asadollah-pour, S. H. Sajjadi, S. N. Nabavi, Investigating photocatalytic degradation of o-nitrophenol and p-nitrophenol over efficient CoO-Fe_2O_3@SiO_2@TiO_2 nanocomposite: rank annihilation factor analysis approach, Chem. Pap. 76 (2022) 427–438.

[39] L. Qin, J. Meng, G. Yang, Y. Pan, X. Gao, Y. Yang, Y. Guo, Interlayer single-atomic Fe−N_4 sites on carbon-rich graphitic carbon nitride for notably enhanced photo-Fenton-like catalytic oxidation processes towards recalcitrant organic micropollutants, App. Catal. B: Environ.

345 (2024) 123695.
[40] D. Wang, M. Wang, Z. Xu, Y. Hu, J. Zhong, T. Ma, Synthesis oxygen vacancies enriched CuO hierarchical nanosheets for peroxymonosulfate activation toward p-nitrophenol degradation and mechanism, Sep. Purif. Technol. 335 (2024) 126262.
[41] Z. Chen, C. Zhao, R. Ma, Z. Yao, Z. Guo, Z. Zhao, Y. Zheng, H. Fu, Interface and polarization engineering of ZIF-67(Co)-based heterojunctions for selective non-Radical PMS activation: simultaneous generation of $^1O_2$ and Co(IV)=O for efficient and safe water remediation, Adv Funct Materials. (2025) e16474.
[42] H. Zhao, Y. Cao, Y. Liu, H. Wang, H. Yu, Efficient degradation of phenol by MnOOH-rGO composite with high peroxymonosulfate utilization efficiency, Chemosphere. 336 (2023) 139200.
[43] A. V. Narendra Kumar, W. S. Shin, Yolk-shell Fe_2O_3@mesoporous hollow carbon sphere hybrid sub-micro reactors for effective degradation of organic contaminants, Chem. Eng. J. 465 (2023) 142922.
[44] X. Wang, D. Liu, Study on photocatalytic degradation of rhodamine B by modified red mud catalyst with biochar, Eur. J. Sustain. Dev. 14 (2025) 877.
[45] X. Wang, G. Liu, Y. Cao, X. Lu, C. Guan, J. Li, J. Ma, J. Jiang, Y. Yang, Efficient degradation and deiodination of iopamidol by synergistic •OH and SO_4•− oxidation in O_3/PMS system, Chem. Eng. J. 521 (2025) 166362.
[46] L. Dong, X. Zhang, W. Xiong, L. Zhou, J. Lei, J. Zhang, Y. Liu, T. P. Nguyen, Enhanced peroxymonosulfate activation via $MnCo_2O_4$/rGO with near-infrared photothermal effect for antibiotics degradation, Eur. J. Inorg. Chem. 28 (2025) e202400856.
[47] Y. Zhao, H. An, G. Dong, J. Feng, T. Wei, Y. Ren, J. Ma, Oxygen vacancies induced heterogeneous catalysis of peroxymonosulfate by Ni-doped $AgFeO_2$ materials: evolution of reactive oxygen species and mechanism, Chem. Eng. J. 388 (2020) 124371.
[48] B.C. De, W. Zhang, C. Yang, A. Mándi, C. Huang, L. Zhang, W. Liu, M.W. Ruszczycky, Y. Zhu, M. Ma, G. Bashiri, T. Kurtán, H. Liu, C. Zhang, Flavin-enabled reductive and oxidative epoxide ring opening reactions, Nat Commun. 13 (2022) 4896.
[49] L. Wang, X. Fu, C. Zhu, X. Xiao, Y. Xu, W. Huang, Z. He, Y. Xia, T. Yang, Y. Gao, Activated charge transfer by interfacial S−O “bridge” at $MnIn_2S_4/WO_3$ for eliminating kanamycin: Z-scheme mechanism, pathways and toxicity assessment, Sep. Purif. Technol. 355 (2025) 129712.
[50] X. Fu, L. Wang, F. Gao, C. Zhu, J. Tao, Z. He, Y. Xia, Z. Zhang, Insight into the synergic charge transfer on S − Mo bond-modified Z-scheme MgInS/MoSe towards norfloxacin degradation: Mechanism, pathways and toxicity evaluation, Fuel. 368 (2024) 131700

Supplementary Files

This is a list of supplementary files associated with this preprint. Click to download.

- supportinginformation.pdf